# 6 Electronic Spectroscopy of the Au-Ne complex

## *6.1 Introduction*

The Au-Ne complex was the fourth Au-RG complex to be studied at Nottingham. Prior to this no work had been reported on this complex, or in fact any coinage metal – Ne complex. From previous work on the Au-RG complexes shown in previous Chapters, a relationship between the polarizability of the RG and the dissociation of the ground state is observed. Xe the most polarizable of the RG's studied, interacted most strongly with the neutral Au atom, whilst Ar, the least polarizable of the RG studied, interacted weakest. It is also observed that as the polarizability of the RG increases, the $D^2\Pi_{1/2}$, $D^2\Pi_{3/2}$ excited states of these RG complexes become increasingly more bound than their corresponding ground state, evidenced by an increased red shift from the associated atomic transition.

There have also been a number of studies, summarized in a review by Bellert and Breckenridge,[1] on the isovalent alkaline earth metal cations complexed with a RG, of which Ne was one. In these studies similar trends observed were also attributed to changes in polarizability, hence significantly weaker bonding was observed in the alkaline earth metal cation -Ne complexes.

In this study the (1+1) REMPI spectra of the $D^2\Pi_{3/2}$ state of the $^{197}$Au-$^{20}$Ne and $^{197}$Au-$^{22}$Ne complexes are reported. The absolute

vibrational numbering is determined, from which experimental spectroscopic constants were derived. High level *ab initio* calculations are employed to characterize the potential energy curves of the ground state and excited states of interest, from which a rationale for the non-observance of the $D^2\Pi_{1/2}$ is given.

### *6.2 Experimental*

The experimental procedure has been described in detail in Chapter 2 so only a brief description of the experiment is outlined here. Au-Ne complexes were generated by pulsing pure Ne, held at a pressure of ~11 bar, over a Au rod held within the LaVa source. Au atoms ablated by the second harmonic of a Nd:YAG laser (Continuum Minilite II) were seeded into the gas pulse which flowed through the cooling channel, before expanding into the high vacuum region of the chamber. The Au-Ne clusters formed in the resulting expansion travelled to the extraction region where they were ionized and detected. The repeller plates used to extract the ions from the ionization region were set at +1150 V and +910 V for the bottom and top plates respectively.

The frequency doubled output of a Sirah dye laser was focused into the extraction region of the ionization chamber leading to ionization of the Au-Ne complexes in a (1+1) REMPI scheme. The dye laser used Coumarin 540A and 480 dyes for investigations into the $D^2\Pi_{1/2}$ and $D^2\Pi_{3/2}$ states respectively and was pumped by the third harmonic of a Surelite III Nd:YAG laser.

## *6.3 Experimental Results and Discussion*

### *6.3.1 Au-Ne $D^2\Pi_{3/2}$ excited state*

In Figure 6.1 the (1 + 1) REMPI spectrum obtained in the region of the Au $^2P_{3/2} \leftarrow {}^2S_{1/2}$ transition for the $^{197}$Au-$^{20}$Ne isotopomer is presented. Figure 6.2 shows a comparison of this spectrum to the corresponding $^{197}$Au-$^{22}$Ne spectrum, clearly displaying the small isotopic shifts observed between the two isotopomers. The peak positions for the features in the two spectra are given in Table 6.1. These were obtained for $v'$ = 0–2 for both isotopomers. However, owing to a combination of a relatively small signal for the $^{197}$Au-$^{22}$Ne isotopomer and the strong atomic Au $6p \leftarrow 6s$ transition, features to higher $v$ were severely affected by the extremely strong, non-resonant $Au^+$ signal from which the MCPs were unable to recover before the $Au^+$–Ne ions arrived; this led to spectra in the latter mass channel which led to unreliable intensities. This problem was less severe for the $^{197}$Au–$^{20}$Ne isotopomer, owing to a greater signal intensity that allowed a background subtraction to be sufficiently effective that features to higher $v$ could be observed. Even so, evidence of this strong atomic resonance still disrupted this region of the spectrum; hence intensities here should be viewed with caution. The determination of the absolute numbering of the vibrational levels was achieved by an analysis of the measured isotopic shifts between the different isotopomers, as performed in Chapters 4 and 5 for Au-Kr and Au-Xe respectivley. The plot obtained for this analysis is shown in Figure 6.3 and clearly suggests that the first observed peak is that of the origin.

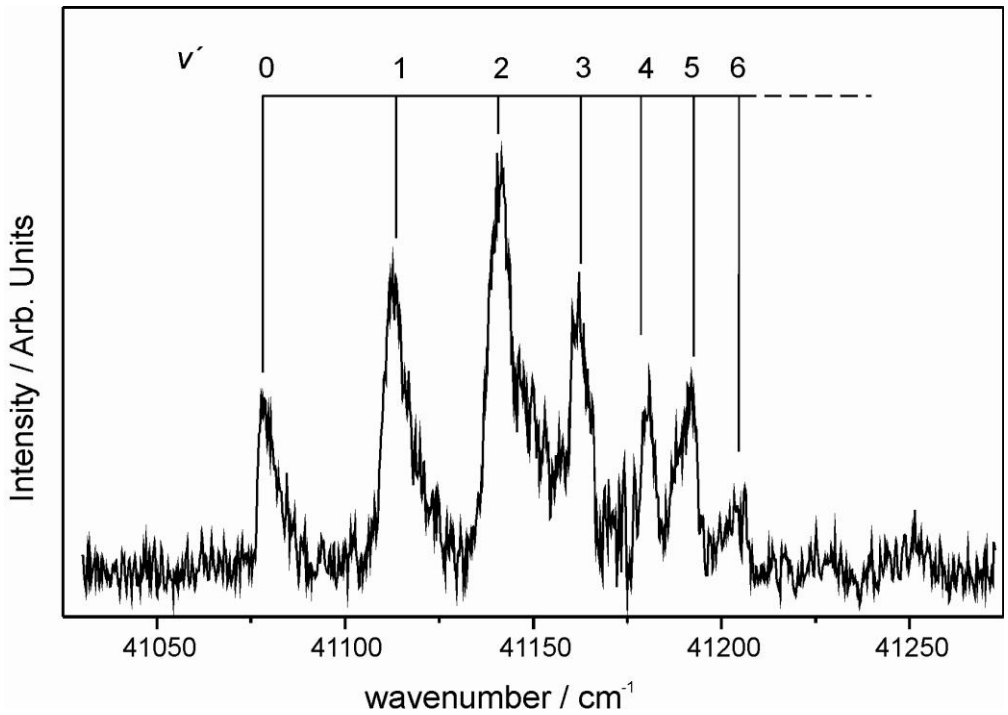


**Figure 6.1. (1+1) REMPI spectrum of $D^2\Pi_{3/2} \leftarrow X^2\Sigma_{1/2}^+$ transition for $^{197}$Au-$^{20}$Ne. The vibrational numbering was determined from an analysis of isotopic shifts between isotopomers (see text).**

Using the absolute vibrational numbering determined, it is possible to deduce a number of spectroscopic constants. Fitting the peak positions to a Morse potential, as shown in Figure 6.4 (a), allows both $\omega_e'$ and $\omega_e'x_e'$ to be obtained, from which $D_e'$ and $D_0'$ can be estimated. $D_0''$ can then be calculated as both the origin transition ($T_0$) and the $6^2P_{3/2} \leftarrow 6^2S_{1/2}$ atomic excitation energy are known. The derived spectroscopic constants are presented in Table 6.2. The Morse potential values suggest that the last bound vibrational level before dissociation is likely to be $v' = 7$, with features up to $v' = 6$ being observed in the spectrum. A LeRoy-Bernstein analysis was additionally performed and is shown in Figure 6.4(b); the derived spectroscopic constants from this analysis are also presented in Table 6.2.

**Table 6.1. Line position ($cm^{-1}$) for features observed for the $D^2\Pi_{3/2} \leftarrow X^2\Sigma_{1/2}^+$ transition.**

| $\upsilon'$ | $^{197}Au$–$^{20}Ne$ | $^{197}Au$–$^{22}Ne$ |
|---|---|---|
| 0 | 41078.8 | 41077.7 |
| 1 | 41113.7 | 41112.1 |
| 2 | 41140.8 | 41137.0 |
| 3 | 41162.2 | - |
| 4 | 41180.8 | - |
| 5 | 41192.0 | - |
| 6 | 41204.4 | - |

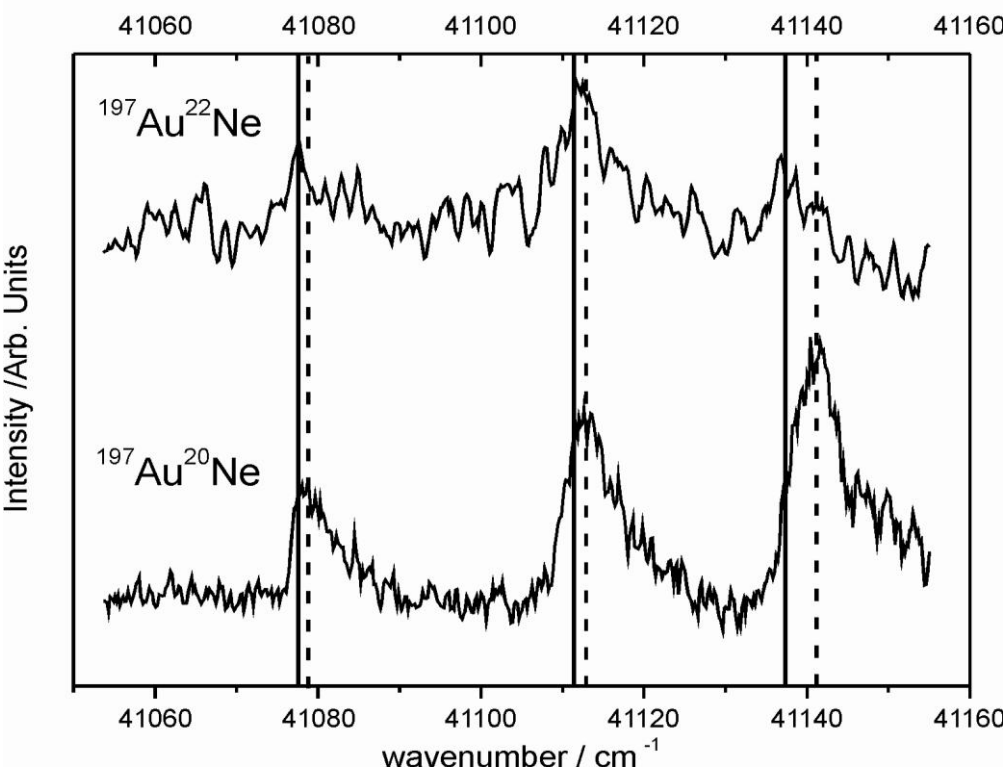


**Figure 6.2. Comparison of $^{197}Au$-$^{20}Ne$ and $^{197}Au$-$^{22}Ne$ spectra for the low-energy ($\upsilon'$ = 0-2) region of $D^2\Pi_{3/2} \leftarrow X^2\Sigma_{1/2}^+$ transition.**

### *6.3.2 Au-Ne $D^2\Pi_{1/2}$ excited state*

After recording the spectrum of the $D^2\Pi_{3/2} \leftarrow X^2\Sigma_{1/2}^+$ transition, the dye in the dye laser was switched so that the region around the $^2P_{1/2} \leftarrow {}^2S_{1/2}$ atomic Au transition could be investigated. No signals attributable to Au–Ne were detected, despite there being a very strong Au atomic signal. The carrier gas was switched to Ar, and

immediately strong signals corresponding to the $D^2\Pi_{1/2} \leftarrow X^2\Sigma_{1/2}^+$ transition of Au–Ar were detected, as previously reported in Chapter 3 and also by Knight *et al.*,[2] which indicated that complexation was occurring satisfactorily. The carrier gas was then switched back to Ne which confirmed that no Au-Ne signal could be detected in this spectral region. The dye was changed back to again allow the region corresponding to the $6^2P_{3/2} \leftarrow 6^2S_{1/2}$ atomic transition to be probed, which immediately enabled the re-recording of the $D^2\Pi_{3/2} \leftarrow X^2\Sigma_{1/2}^+$ spectrum of Au–Ne. The conclusion from these studies is that the $D^2\Pi_{1/2}$ state of Au–Ne is very weakly bound and/or the Franck-Condon factors are very small in this region.

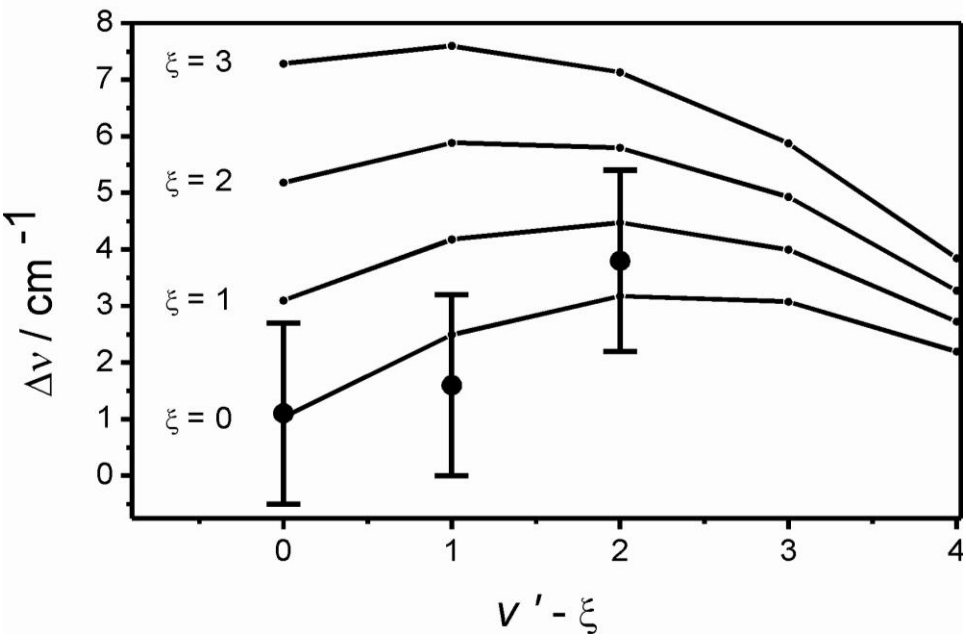


**Figure 6.3. Calculated (lines with small circles) and experimental (large circles, with error bars) isotopic shifts between vibrational energy levels in $^{197}$Au–$^{20}$Ne and $^{197}$Au–$^{22}$Ne, for various absolute numberings, where the $v'$ - ξ value labels the observed features. Centres of the asymmetric bands have been estimated.**

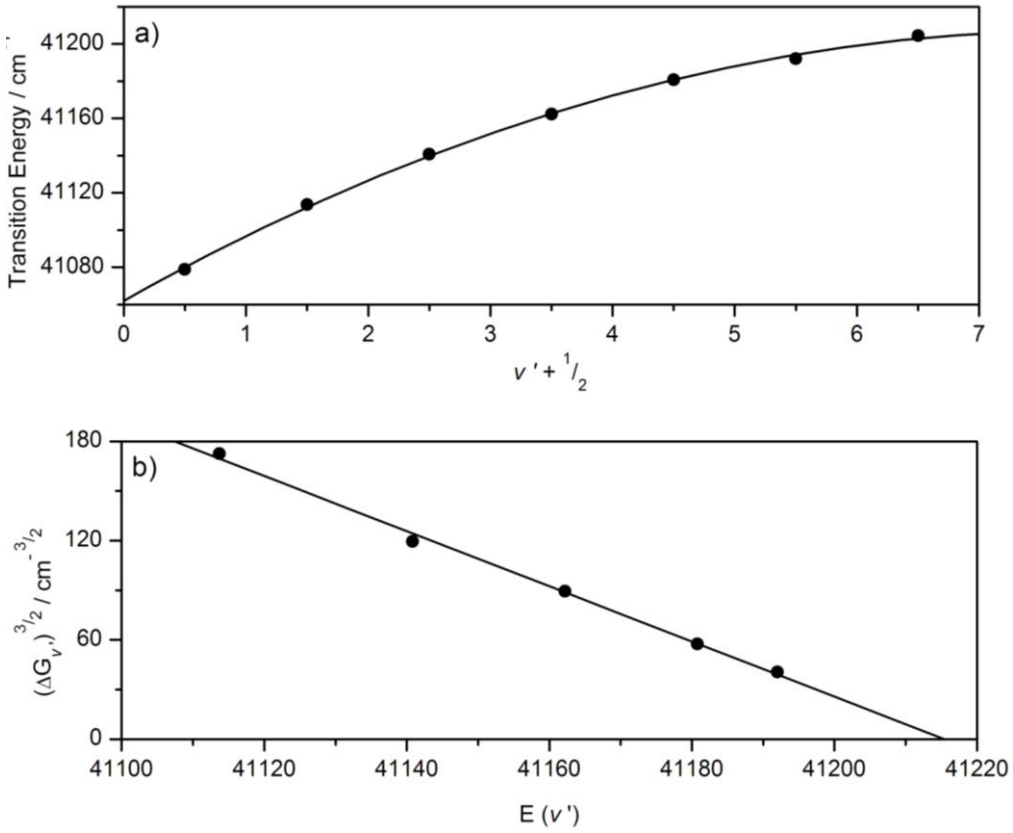


**Figure 6.4. Morse analysis (a) and LeRoy-Bernstein analysis (b) of vibrational features observed for the $^{197}$Au-$^{20}$Ne $D^2\Pi_{3/2}$ state.**

**Table 6.2. Derived spectroscopic constants (cm$^{-1}$) for the $^{197}$Au-$^{20}$Ne $D^2\Pi_{3/2}$ state.**

| | Morse | LeRoy-Bernstein |
|---|---|---|
| $\omega_e$ | 36.9 | --- |
| $\omega_e x_e$ | 2.35 | --- |
| $D_e'$ | 145.1 | 153.9[a] |
| $D_0'$ | 127.8 | 136.0 |
| $D_0''$ | 31.4 | 40.0 |

[a] Estimated from the $D_0'$ value and using the Morse potential vibrational constants.

## *6.4 Computational methodology*

Calculations on the $X^2\Sigma_{1/2}^+$ ground state and the molecular states arising from the Au($^2D_J$) + Ne($^1S$) and Au($^2P_J$) + Ne($^1S$) asymptotes, similar to those for Au-Ar described in detail in Chapter 3, were performed for Au-Ne. All calculations were again performed with MOLPRO[3] by other members of the research group.

### *6.4.1 Au-Ne $X^2\Sigma_{1/2}^+$ state*

A potential energy curve for the $X^2\Sigma_{1/2}^+$ state was calculated pointwise at the RCCSD(T) level. For Ne the *d*-aVXZ (X = Q, 5) basis sets were employed, while for Au the small core relativistic effective core potential, ECP60MDF[4] was employed, to which the *d*-aug-cc-pVXZ-PP (X = Q, 5) basis set was added. These RCCSD(T) calculations were performed using the frozen core approximation in which all but the 1*s* electrons of Ne and the ECP electrons in Au were correlated. Each point was corrected for basis set superposition error using the full counterpoise correction,[5] and then extrapolated to the basis limit using the two point extrapolation procedure of Helgaker and co-workers.[6,7] The potential energy curves were used as input for the LEVEL program[8] as described for Au-Ar. The $^{197}$Au and $^{20}$Ne isotopes were used for all calculations; the results of these analyses are shown in Table 6.3.

**Table 6.3. Calculated spectroscopic constants, and 0-1 and 1-2 vibrational intervals for the $X^2\Sigma_{1/2}^+$ state of $^{197}$Au-$^{20}$Ne at the RCCSD(T) level of theory.**

| Basis Set | $R_e$/ Å | $D_e$/ cm$^{-1}$ | $D_0$/ cm$^{-1}$ | 0-1 / cm$^{-1}$ | 1-2/ cm$^{-1}$ | $B_0$/ cm$^{-1}$ |
|---|---|---|---|---|---|---|
| *d*-aVQZ | 3.840 | 46.2 | 37.0 | 15.0 | 10.7 | 0.05989 |
| *d*-aV5Z | 3.834 | 46.7 | 37.5 | 15.1 | 10.9 | 0.06008 |
| *d*-aV∞Z | 3.826 | 47.2 | 38.0 | 15.1 | 11.0 | 0.06029 |

### *6.4.2 Au-Ne excited state calculations*

The calculations on the excited states of Au-Ne were carried out in a similar manner to those on Au-Ar described in detail in Chapter 3. Initially, single point, single reference RCCSD(T) calculations employing *d*-aug-cc-pVDZ-PP basis sets, were performed to determine where the states arising from the Au($^2D$) + Ne($^1S$) asymptote cross the

higher lying $^2\Pi$ and $^2\Sigma^+$ states arising from the Au($^2P$) + Ne($^1S$) asymptote. The calculated potential energy curves can be seen in Figure 6.5. As in the other complexes, it can be seen that the states are well separated in energy, suggesting that a single reference method is adequate for the states considered; confirmed by a $T_1$ diagnostic value of less than 0.031. Again the two states considered (see Chapter 3) arising from the Au($^2D$) + Ne($^1S$) asymptote are almost indistinguishable on the scale of the figure and as such it is expected that the omitted $C^2\Sigma^+$ state will follow these states closely. The most important result of these calculations is that the states arising from the Au($^2D$) + Ne($^1S$) asymptote only cross the higher lying $D^2\Pi$ states high on their repulsive limb, and hence any observable effect on the $D^2\Pi$ states will be minimal. The $E^2\Sigma^+$ state, which like the $D^2\Pi$ states also arises from the Au($^2P$) + Ne($^1S$) asymptote, was excluded from these calculations, but is located above the $D^2\Pi$ states and is therefore also not expected to be affected by crossings from the lower lying $A^2\Delta$, $B^2\Pi$ and $C^2\Sigma^+$ states.

In order to compare to the experimental results more reliably, the $D^2\Pi$ potential energy curve was recalculated at the RCCSD(T)/*d*-aVQZ level, performing the full counterpoise correction at each internuclear separation. It should be noted that the effect of the inclusion of SO interaction in the calculations for this state is just expected to shift the $D^2\Pi_{3/2}$ curve up by a constant amount, $\zeta/2$, where $\zeta$ is the atomic spin orbit coupling constant for the Au($6^2P$) state. Analysis of this curve yielded spectroscopic constants of $R_e'$ = 3.083 Å, $D_e'$ = 167.7 cm$^{-1}$, $D_0'$ = 147.1 cm$^{-1}$, $\omega_e'$ = 42 cm$^{-1}$ and $\omega_e'x_e'$ = 3.0 cm$^{-1}$. A single-

point RCCSD(T)/*d*-aV5Z at this $R_e'$ value yielded a $D_e'$ value of 172.8 $cm^{-1}$, which extrapolates to a basis set limit value of 178.2 $cm^{-1}$, which gives a $D_0'$ value of 157.6 $cm^{-1}$. These values are in fairly good agreement with the experimental values for the $D^2\Pi_{3/2}$ state reported in Table 6.2.

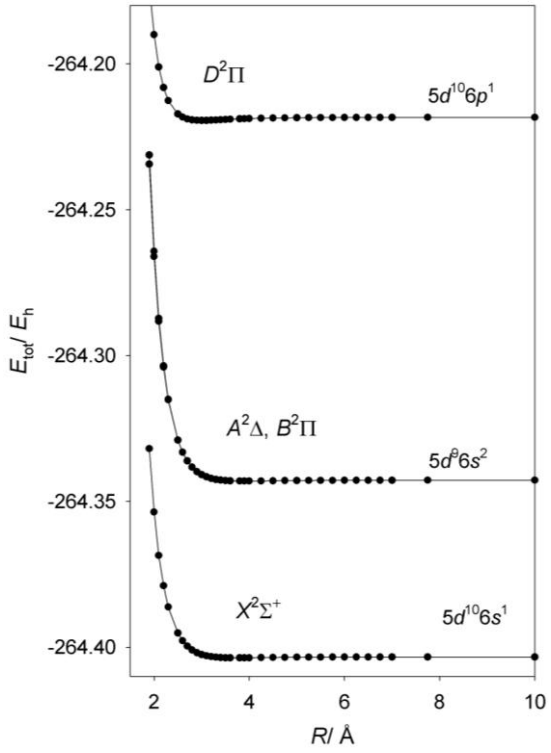


**Figure 6.5. Calculated RCCSD(T)/aVQZ potential energy curves for the *X*, *A*, *B* and *D* states of Au–Ne. Note that the *A* and *B* states cannot be resolved from each other on this scale, and the *C* state (not calculated) would also be expected not to be resolvable. The *E* state, also not included, lies to higher energy (see Figure 6.6)**

As in previous work, a set of CASSCF+MRCI calculations, with an aug-cc-pVQZ basis set, including the Davidson correction (+Q) where the 5*d* and lower orbitals of Au were constrained to remaining doubly occupied were performed. That is, only the unpaired 6*s* or 6*p* electron was allowed to be active in the calculations for the respective states. However, the doubly-occupied orbitals were allowed to relax during

the CASSCF procedure. This will, of course, limit the amount of dynamic correlation included; however, this is satisfactory since only a qualitative picture is needed. Since the CASSCF treatment does not consider the same set of orbitals for the $^2\Sigma^+$ and $^2\Pi$ states (because of the different symmetry), the calculated asymptotic energies were not precisely equal for the $D^2\Pi$ and $E^2\Sigma^+$states.

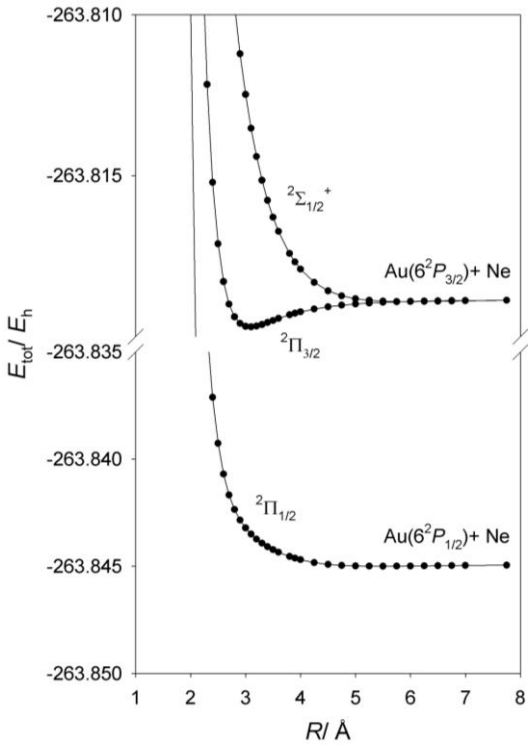


**Figure 6.6. CASSCF+MRCI+Q/aVQZ calculations for the $D^2\Pi_{1/2}$, $D^2\Pi_{3/2}$ and $E^2\Sigma_{1/2}{}^+$ states of Au-Ne.**

In the previous Chapters the Davidson-corrected CASSCF + MRCI energies of the two $^2\Pi$ states and the $E^2\Sigma^+$ state were used as the unperturbed energies in state-averaged CASSCF spin-orbit calculations, to determine the spin orbit coupling at each *R*. However, this resulted in a calculated separation value for the spin-orbit split asymptotes of 2500-2600 cm$^{-1}$, considerably lower than the $6^2P_{3/2}$–$6^2P_{1/2}$ atomic splitting of $^3/_2\zeta$ = 3815.4 cm$^{-1}$ (known from atomic

spectroscopy).[9] Although it would be possible to extend these calculations, it has not been done here as a fuller theoretical treatment ought to include a full account of spin-orbit coupling, and hence possible couplings with other $\Omega = {}^{3}/_{2}$ states, and perhaps allowing for relaxation of the spin-orbit wavefunctions. Therefore, in the present work analytic expressions (together with the above value of $\zeta$) which link the $^2\Sigma^+$ and $^2\Pi$ states to the spin-orbit states, have been used, the derivation of which are included in the appendix of reference 10. Again, there is a slight non-degeneracy in the $^2\Sigma^+$and $^2\Pi$ states at the asymptotes, and so the $^2\Pi$ state is shifted to match the asymptotic energy of the $^2\Sigma^+$ state prior to employing the analytic expressions. The resulting curves are presented in Figure 6.6.

## *6.5 Discussion*

### *6.5.1 Non-observance of the $D^2\Pi_{1/2}$ state*

In previous studies on Au-RG complexes, spectra corresponding to the $D^2\Pi_{1/2} \leftarrow X^2\Sigma_{1/2}^+$ transition have been observed; however, no Au-Ne signal was detected when scanning the appropriate energetic region in this study. Examination of the spin-orbit interaction energy curves for Au–Ne, shown in Figure 6.6, provides an explanation for this observation. Whilst the non-spin-orbit $D^2\Pi$ state is, as expected, fairly well bound owing to the location of the unpaired electron off-axis, mixing of the $D^2\Pi_{1/2}$ component with the very weakly-bound $E^2\Sigma_{1/2}^+$ state can cause severe changes in the binding of the resulting states, as observed for Au–Ar, Au–Kr and Au–Xe. It can be seen from Figure 6.6 that the mixing in of the repulsive region of the $E^2\Sigma_{1/2}^+$ state has

led to a very shallow well in the lower component with a minimum at ~ 5.0 Å. Given the minimum in the *X* state is at ~3.8 Å (Table 3), it is unsurprising that there is no observed spectrum in this region; as any such transitions will have a small Franck-Condon factor (FCF), and likely access the repulsive region of the $Au^+$–Ne potential curve, and hence yield $Au^+$ ions, however, which would be lost in the persistent, large non-resonant $Au^+$ signal. On the other hand the minimum of the $^2\Pi_{3/2}$ state is at 3.08 Å, leading to much higher FCFs.

### *6.5.2 FCF Simulation of the $D^2\Pi_{3/2} \leftarrow X^2\Sigma_{1/2}^+$ spectrum*

Franck-Condon simulations were performed for the $D^2\Pi_{3/2} \leftarrow X^2\Sigma_{1/2}^+$ spectrum by fixing the ground state geometry and vibrational parameters to those obtained at the RCCSD(T)/*d*-aV∞Z level of theory, shown in Table 6.3. The $R_e'$ = 3.08 Å value used for the excited state is that determined from the CP-corrected RCCSD(T)/*d*-aVQZ calculations for the non-spin-orbit $D^2\Pi$ state (expected to be the same as for the $D^2\Pi_{3/2}$ state), which is used in conjunction with the experimentally-derived $\omega_e'$ and $D_e'$ values for the $D^2\Pi_{3/2}$ state. It was expected that the experimental intensities in the centre of the spectrum were likely unreliable, particularly for $v'$ = 3, 4. This was owing to the effects of subtracting out the large persistent Au signal, in addition to the most intense features becoming saturated at the higher laser powers required to observe the weaker features. It was therefore decided to scale the spectrum to match the experimental intensity for the first band as this was the least likely to be saturated, the resulting simulated spectrum is shown in Figure 6.7. It is interesting to note

that despite the intensity of the simulated features in the centre of the spectrum being considerably greater than that of experimental features, to higher energies the simulated features are considerably weaker, reminiscent of what was observed for Au-Ar in Chapter 3. A possible explanation for this may be that as the asymptote is approached further configurational and spin-orbit mixings occur, leading to this rise in intensity. As noted above, the $D^2\Pi_{3/2}$ state should not mix with any other states to first order. However, there are $\Omega = {}^3/_2$ states arising from the lower Au($5^2D$) + RG($^1S$), and the higher Au($^4P_{5/2}$) + RG($^1S$) and Au($7p$) + RG($^1S$) asymptotes, amongst others, which may be affecting the intensity of the spectra to long $R$ by such mixing.

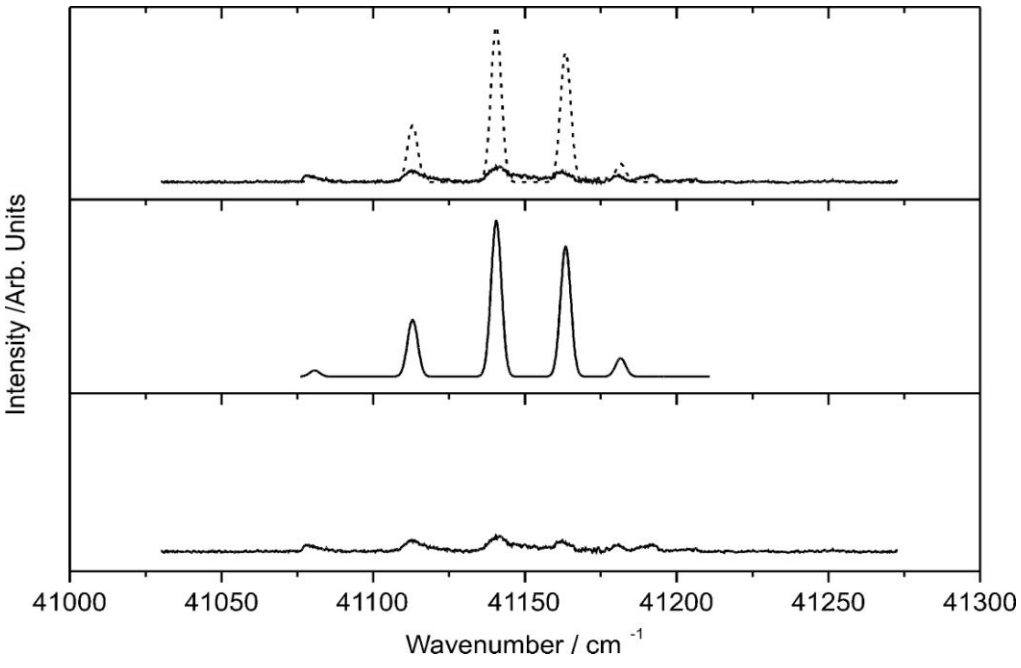


**Figure 6.7. Franck-Condon simulation of the $D^2\Pi_{3/2} \leftarrow X^2\Sigma_{1/2}^+$ transition for $^{197}$Au–$^{20}$Ne, using parameters from the ab initio calculations reported (see text). The intensities of the simulated spectrum have been scaled so that the $v' = 0$ intensity matches the experimental one.**

The rotational profiles of the vibrational features observed for the $D^2\Pi_{3/2} \leftarrow X^2\Sigma_{1/2}^+$ transtion were simulated using the $B_v'$ values from the analysis of the RCCSD(T)/d-aVQZ potential and the $B_0''$ value from the $X$ state. Since individual rotational lines were not resolved, a Gaussian line profile, with the full width at half maximum (FWHM) set at 0.8 $cm^{-1}$ was used; the best-fit to the profile over the whole series was with a rotational temperature of 15 K. Note that vibrational hot bands were not apparent in the spectrum, and so there is no information on the vibrational temperature. Owing to the difficulties in reproducing the experimental intensities in FCF calculations, as noted above, each computed vibrational band was scaled to match the experimental intensity. The resulting spectrum is given in Figure 6.8 where the change in rotational profile undergoing a distinct change from blue to red shading as $v$ increases is well reproduced.

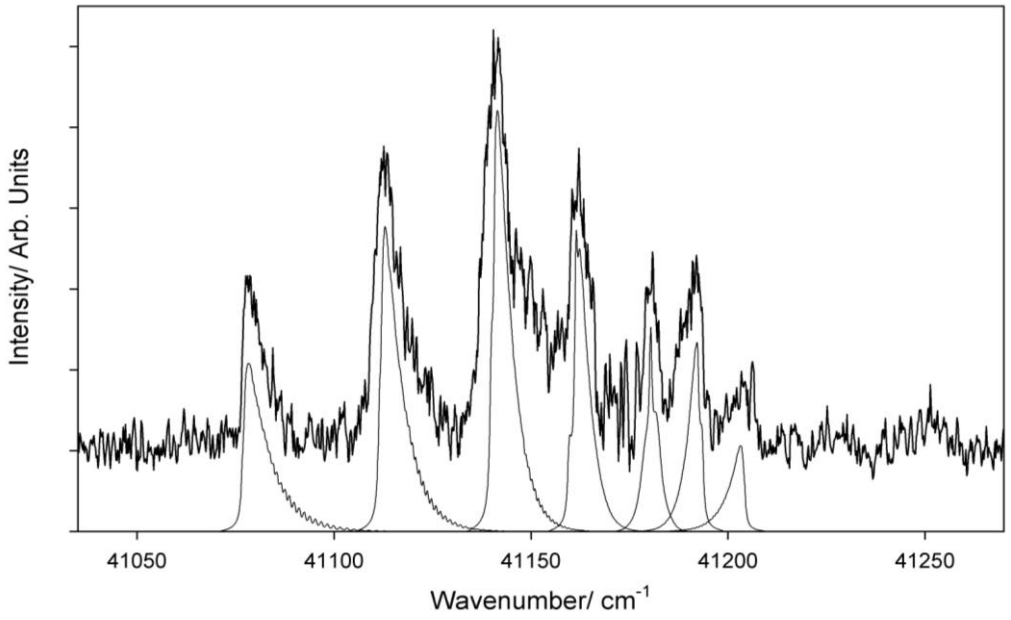


**Figure 6.8. Simulated rotational profiles for the vibrational features of the $D^2\Pi_{3/2} \leftarrow X^2\Sigma_{1/2}^+$ transition for $^{197}Au$-$^{20}Ne$.**

### *6.6 Conclusions*

The Au-Ne complex was investigated in the energetic region corresponding to Au $^2P_J \leftarrow {}^2S_{1/2}$ (where $J = {}^1/_2, {}^3/_2$) atomic transitions. Features were observed corresponding to the $D^2\Pi_{3/2} \leftarrow X^2\Sigma_{1/2}^+$ transition for both the $^{197}$Au-$^{20}$Ne and $^{197}$Au-$^{22}$Ne isotopomers from which the absolute vibrational numbering and hence a number of spectroscopic parameters, could be derived.

The non-observance of the $D^2\Pi_{1/2}$ state, which was also expected to be in a similar energetic region, was rationalized using the results of high level *ab initio* calculations. These calculations suggest that mixing of the $D^2\Pi_{1/2}$ state with the $E^2\Sigma_{1/2}^+$ state through spin-orbit interactions, as observed in Au-Ar, results in an extremely weakly bound $D^2\Pi_{1/2}$ state whose potential minimum resides outside the Franck-Condon window.

Results of additional calculations were used in conjunction with experimentally derived spectroscopic constants, which were used to conduct FCF simulations. From these simulations it has been postulated that the intensity of the higher energy features of the $D^2\Pi_{3/2}$ state experimental spectrum are enhanced owing to an increased configurational and spin-orbit mixing as the asymptote is approached; thus also providing an explanation for similar observations for Au-Ar. In addition the changing rotational profile of the peaks has been successfully simulated, strengthening the validity of the calculations and suggesting a rotational temperature of ~15 K.

***References***


[1] D. Bellert and W. H. Breckenridge, *Chem. Rev.* 2002, **102**, 1595.

[2] A. M. Knight, A. Stangassinger and M. A. Duncan, *Chem. Phys. Lett.* 1997, **273**, 265.

[3] MOLPRO is a package of *ab initio* programs written by H. J. Werner, P. J. Knowles and others.

[4] D. Figgen, G. Rauhut, M. Dolg, and H. Stoll, *Chem. Phys.*, 2005, **311**, 227.

[5] S. F. Boys, F. Bernardi, *Mol. Phys.,* 1970, **19**, 553.

[6] T. Helgaker, W. Klopper, H. Koch and J. Noga, *J. Chem. Phys.*, 1997, **106**, 9639.

[7] A. Halkier, T. Helgaker, P. Jỳrgensen, W. Klopper, H. Koch, J. Olsen and A. K. Wilson, *Chem. Phy. Lett.*, 1998, **286**, 243.

[8] R. J. LeRoy, LEVEL 7.2 - A computer program for solving the radial Schrödinger equation for bound and quasibound levels, and calculating various expectation values and matrix elements. (University of Waterloo Chemical Physics Research Program Report CP-555R (2000)).

[9] J. C. Ehrhardt and S. P. Davis, *J. Opt. Soc. Am.*, 1971, **61**, 1342.

[10] R. J. Plowright, A. M. Gardner, C. D. Withers, T. G. Wright, M. D. Morse and W. H. Breckenridge, *J. Phys. Chem. A*, 2010, **114**, 9, 3103.